Correspondence to:
X. Shang,
xdshang@scsio.ac.cn

Strength and Spatial Structure of the Perturbation Induced by a Tropical Cyclone to the Underlying Eddies

Zhumin Lu[1,2,3] (ID), Guihua Wang[4,5] (ID), and Xiaodong Shang[1,2,3] (ID)

[1]State Key Laboratory of Tropical Oceanography, South China Sea Institute of Oceanology, Chinese Academy of Sciences, Guangzhou, China, [2]Southern Marine Science and Engineering Guangdong Laboratory (Guangzhou), Guangzhou, China, [3]Institution of South China Sea Ecology and Environmental Engineering, Chinese Academy of Sciences, Guangzhou, China, [4]Department of Atmospheric and Oceanic Sciences and Institute of Atmospheric Sciences, Fudan University, Shanghai, China, [5]CMA-FDU Joint Laboratory of Marine Meteorology, Fudan University, Shanghai, China

Abstract A tropical cyclone (TC) induces the oceanic geostrophic response, which perturbs the underlying ocean eddy field. This study investigates the strength and spatial structure of isopycnal undulations and potential vorticity (PV) changes linked with the geostrophic response by use of a linear, two-layer theory and an OGCM. It is found that the strength and cross-track length scale of the geostrophic response are well compared with those of background eddies, highlighting the ability of a TC to perturb underlying ocean eddies. More importantly, the TC-induced PV perturbation is confined within the thermocline between 100 and 300 m depth, causing the 3D quasi-geostrophic evolution of the perturbed eddies. The length scale of upwelling perturbation (which is ~130 km) is larger than that of PV response (~50 km). This scale disparity means that the patterns of the TC-induced perturbations are subject to eddy-TC separation distance. Consequently, the perturbation of a TC to an eddy is significant (negligible) when the eddy-TC separation distance is less than 80 km (larger than 200 km). This study provides a starting point for understanding the TC-induced 3D evolution of the perturbed ocean eddy field.

1. Introduction

Roughly 80 tropical cyclones (TCs), that is, hurricanes and typhoons, are generated each year in tropical oceans (Emanuel, 1991). When moving toward high latitude, TCs inject significant perturbations to the underlying mesoscale ocean eddy field. In addition to inducing the near-inertial response (Greatbatch, 1984; Meroni et al., 2017; Niwa & Hibiya, 1997), it is well known that TCs also induce the geostrophic response (Geisler, 1970; Price, 1983). However, the geostrophic response is usually ignored because the power injected by a TC into it is far smaller than that injected into the near-inertial response (Nilsson, 1995; Price, 1983). Using satellite altimetry data and an OGCM, Lu et al. (2016; hereafter LWS) revealed that a typhoon with a moving speed of 13.2 km hr^{-1} causes substantial increases in the amplitude and size of an underlying cyclonic ocean eddy (COE). This significant change is attributed to the geostrophic response induced by the typhoon. Thus, investigating the details of the TC-induced geostrophic response, such as its strength and spatial structure, is vital to improve our understanding of the interaction between TCs and the underlying ocean eddy field.

The geostrophic response consists of both barotropic and baroclinic components (Geisler, 1970) with rather weak coupling (Ginis & Sutyrin, 1995). The nature of the barotropic geostrophic response is characterized by a broad along-track sea surface height (SSH) trough along with the weak geostrophic currents (Geisler, 1970; Ginis & Sutyrin, 1995). In a deep open ocean, the strength of the barotropic component is quite weak and essentially ignorable, so that the geostrophic response can be assumed to be principally baroclinic (Ginis, 2002; Ginis & Sutyrin, 1995). The baroclinic geostrophic response manifests as a persistent thermocline ridge in geostrophic balance with the induced currents (Geisler, 1970). In contrast to the much weaker barotropic SSH trough, a strong along-track baroclinic SSH trough accompanies the thermocline ridge. Since barotropic signals propagate too fast to be fully captured by satellite altimetry, the baroclinic SSH trough in an open ocean comprises the altimetry-based observable signal in the data. For example, Figure 1 shows the SSH trough induced by Typhoon Lupit reported in LWS and its subsequent evolution. In principle, the SSH response is the combination of the near-inertial and geostrophic components. However, considering that near-inertial waves are (1) largely filtered away in the gridded, time-delayed data (Dibarboure et al., 2010)
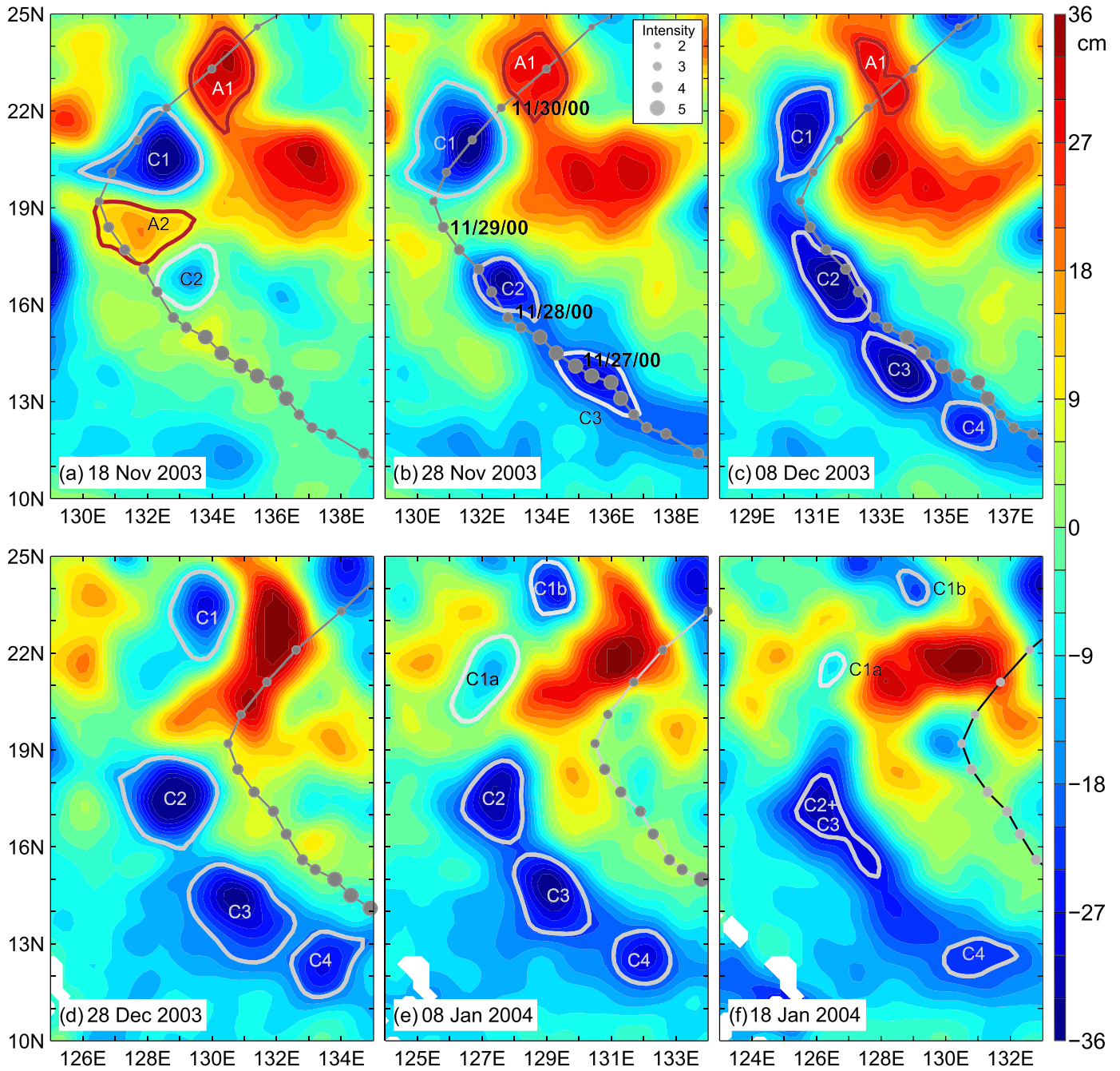
Figure 1. SSH field prior and later to northwest Pacific Typhoon Lupit. The time of the typhoon is labeled in month/day/hour and the intensity of the typhoon is shown in (b). Among the eddies, C1, C2, A1, and A2 are preexisting prior to the typhoon while C3 and C4 are generated by the typhoon. A2 is killed by the typhoon while C1 splits into two COEs (C1a and C1b) finally. The TC-induced geostrophic wakes move westward as Rossby waves, suggesting that β-induced quasigeostrophic motion is an important component dominating the post-TC evolution of geostrophic wakes although the evolution is not discussed in this paper.

and (2) typically disperse away from their source location within 2 weeks (Jaimes & Shay, 2010; Shay & Elsberry, 1987), the SSH trough visible in Figure 1 is largely the signature of the geostrophic response to the typhoon. As seen in Figure 1, a profusion of eddy activity appears subsequent to the typhoon, which includes the total disruption of two preexisting anticyclonic eddies (AOEs; A1 and A2), the elliptical deformation of two COEs (C1 and C2), and the generation of two new COEs (C3 and C4). The evolution

of the isolated COE in LWS is in fact one of the specific cases listed herein (C2). To summarize, the width and strength of the SSH trough is found to be crucial to the subsequent evolution of any perturbed eddies.

It has been observed that a TC can cause SSH depressions of up to 20–60 cm in satellite altimeter data (Ginis, 2002; Kudryavtsev et al., 2019), which has also been simulated in numerical ocean models (Shay et al., 1990). In spite of the strong near-inertial contributions to these SSH depressions, geostrophic components, as shown in Figure 1, are also believed to be considerable. By combining altimetry-based and Argo observations, Sun et al. (2012) showed that Typhoon Namtheun led to an SSH depression of 6 cm and a simultaneous thermocline cooling of 0.5 ~ 1.0 °C. Sun et al. (2012) also found that these signals last at least 15 days, providing in situ observational evidence of the baroclinic geostrophic response. Given that the mean amplitude of global mesoscale eddies is 8 cm (Chelton et al., 2011), all of the above-mentioned TC-induced SSH depressions were likely comparable to the amplitude of the underlying eddies. In the field of eddy-TC interaction, a great deal of attention has been paid to the modulation of preexisting eddies on the upper ocean thermal response and on the TC intensity (Jaimes & Shay, 2009; Jaimes & Shay, 2015; Lin et al., 2005; Shay et al., 2000; Zheng et al., 2010). However, very little work has been devoted to the long-term effects of a TC on the underlying eddies.

The few studies that have investigated the change of a COE caused by a TC were based on remote sensing (Shang et al., 2015; Sun et al., 2014; Walker et al., 2014). These studies mainly focused on using the change in the SSH signals to describe the kinematic change of eddy features such as amplitude, size, and eddy kinetic energy. From satellite observations, it is generally accepted that a slow-moving or more intense TC can enhance and enlarge the underlying COEs. Apart from the change of horizontal eddy features, the vertical structure of a preexisting eddy can also be modified by a TC. As revealed in Gordon et al. (2017), a TC causes a sharp decrease in the AOE amplitude and forms an intra-thermocline eddy in 30–150 m depth range.

Traditionally, a TC was thought to not inject PV into the underlying thermocline (Gill, 1984; Price, 1983). However, as shown in LWS, PV injection played a key role in the simulated evolution of the perturbed COE. It is well known that near-inertial waves do not carry PV, but geostrophic motions do (Pedlosky, 2003). Hence, the geostrophic response induced by a TC must inject PV into thermocline. Therefore, to observe TC-induced contributions of the order of the eddy amplitudes necessitates that TC-induced PV injection has the same order magnitude as those of underlying eddies. To verify this, below we compare the strength and vertical distribution of TC-induced PV signals with those of a background COE and/or AOE. Even if the TC-induced PV injection is not strong enough to significantly affect a preexisting eddy, its perturbation to preexisting PV distribution is still important because PV pattern plays a vital role in investigating the stability of an eddy (Carton, 2001). For example, if the PV of a preexisting eddy (COE or AOE) is homogenized, the eddy becomes stable and penetrates more below the thermocline (Benilov, 2005; Cohen et al., 2015; Cohen et al., 2016).

The principal goal of this study is to quantitatively illustrate strength, cross-track length scale, and vertical range of upwelling and PV linked with the baroclinic geostrophic response induced by a TC by both linear theory and OGCM simulations. Hereafter, if not stated otherwise, every variable refers to its baroclinic geostrophic component. In section 2, we first present the strength and cross-track length scale of the geostrophic response based on a two-layer theoretical model. Section 3 describes the OGCM and methodology. Section 4 analyzes the strength and spatial structure of the response in the OGCM simulations and compares them with background eddies. Section 5 employs a conceptual model to illustrate how the spatial structure of the geostrophic response dominates the quasi-geostrophic evolution of the perturbed eddies. Finally, the results are summarized and the study conclusions are provided in section 6.

2. Strength and Length Scale of the Response in a Two-Layer Theoretical Model

2.1. Governing Equations

A method to estimate the barotropic and baroclinic geostrophic response to external forcing has been presented by Geisler (1970). However, Geisler (1970) applied either an impulse forcing at the TC center or a block forcing along the track to simulate the action induced by a TC. Therefore, his results cannot completely reflect the strength and length scale of the response driven by a real TC. For example, Ginis and

Sutyrin (1995) found that by using an impulse forcing the resulting length scale of the barotropic response is far broader than the size of the TC, while the response forced by a real TC was confined to a limited width. Based on the theoretical framework of Geisler (1970), we will isolate the governing equation for the geostrophic response and analytically solve for the geostrophic response forced by more realistic TC forcing. Our emphasis is placed on studying the strength and the cross-track length scale of upwelling and PV signals.

Assuming that a TC with fixed intensity moves westward at a constant speed U, in the TC-centered coordinate system with $x = Ut$, the TC is fixed and the ocean moves eastward. Then we can write out the two-layer baroclinic mode equation on an f plane to determine the linear TC-induced interface undulations:

$$\left[\frac{1}{C^2} \left(\frac{\partial}{\partial t} + U \frac{\partial}{\partial x} \right)^2 - \left(\frac{\partial^2}{\partial x^2} + \frac{\partial^2}{\partial y^2} \right) + \frac{1}{L_d^2} \right] w = \frac{f}{\rho C^2} curl_z \tau \ , \tag{1}$$

where $curl_z \tau \equiv \partial \tau_y / \partial x - \partial \tau_x / \partial y$ is the wind stress curl of the TC winds, f is the Coriolis parameter, ρ is the seawater density, w is the vertical velocity of the interface, C is the baroclinic mode wave speed, $L_d = C/f$ is the deformation radius ($C = \sqrt{g' H_1}$, where g' is the reduced gravity), and H_1 is the unperturbed interface depth of the first layer. These parameters are chosen according to the case in LWS. The isopycnal $\sigma = 24$ ($H_1 \approx 150 \ m$) was chosen as the location of the two-layer interface. Based on the method in Jaimes and Shay (2009), C is estimated to be 2.13 m s^{-1} and $L_d = 51.4$ km. Equation 1 is the same as Equation 10 in Geisler (1970), in which both mixed layer processes and air-sea heat exchange are omitted. The interface undulation, h, of the total response is then determined by

$$h = \int_{-\infty}^{t} w dt. \tag{2}$$

In the treatment of Geisler (1970), the geostrophic response is the limit of 2 for $t \to \infty$. However, this limit can only be analytically obtained for a block forcing (Geisler, 1970) and not for a more realistic forcing. To resolve this problem, we first isolate the equation controlling geostrophic response and analytically solve the response to a realistic forcing.

First, we integrate 1 from $-\infty$ to t and substitute 2 into it. Then the governing equation for h can be gained:

$$\left[\frac{1}{C^2} \left(\frac{\partial}{\partial t} + U \frac{\partial}{\partial x} \right)^2 - \left(\frac{\partial^2}{\partial x^2} + \frac{\partial^2}{\partial y^2} \right) + \frac{1}{L_d^2} \right] h = \int_{-\infty}^{t} \frac{f}{\rho C^2} curl_z \tau dt. \tag{3}$$

Price et al. (1994) divided the TC-induced response into two stages: the forced and relaxation stages. If the TC forcing occurs over the time interval $[-t_0, t_0]$, the geostrophic response (as well as the total response) must be generated during this interval. Therefore, in the relaxation stage, (i.e., $t > t_0$), Equation 3 becomes

$$\left[\frac{1}{C^2} \left(\frac{\partial}{\partial t} + U \frac{\partial}{\partial x} \right)^2 - \left(\frac{\partial^2}{\partial x^2} + \frac{\partial^2}{\partial y^2} \right) + \frac{1}{L_d^2} \right] h = \int_{-t_0}^{t_0} \frac{f}{\rho C^2} curl_z \tau dt. \tag{4}$$

On the f plane, once the geostrophic response is generated, it does not evolve with t. Furthermore, it should be the same everywhere along the track for the same forcing. For $t > t_0$, applying $\partial(\cdot)/\partial t = 0$ and $\partial(\cdot)/\partial x = 0$ to 4, we can isolate the governing equation for the geostrophic component from the total response,

$$-\frac{\partial^2 h}{\partial y^2} + \frac{1}{L_d^2} h = \frac{f}{\rho U C^2} \int_{-Ut_0}^{Ut_0} curl_z \tau dx. \tag{5}$$

The quasi-geostrophic streamfunction in a two-layer model is defined as (Carton, 2001)

$$\psi = -g' h / f.$$

Therefore, 5 can be written as

$$Q = \frac{\partial^2 \psi}{\partial y^2} - \frac{1}{L_d^2} \psi = \frac{1}{\rho U H_1} \int_{-Ut_0}^{Ut_0} curl_z \tau dx, \tag{6}$$

where Q is the quasi-geostrophic potential vorticity of the response in the upper layer (Carton, 2001). Equation 6 theoretically confirms that the geostrophic response is associated with a positive PV injection into the underlying thermocline. As seen from 6, the strength of TC-injected PV is determined by the moving speed of the TC and its wind stress curl, while the cross-track length scale depends only on the width of positive TC wind stress curl.

2.2. Ekman Layer in the Upper Layer

Ginis and Sutyrin (1995) hypothesized that physically, the baroclinic geostrophic response is generated by the steady component of upwelling associated with the Ekman transport induced by along-track wind stresses. We envision that an Ekman layer with thickness $H_e < H_1$ exists in the upper layer. In the forced response, where the motion is controlled by wind-driven currents (Price et al., 1994), the momentum equation of Ekman layer based on Gill (1982) is given by

$$\frac{\partial(u_e + iv_e)}{\partial t} + if(u_e + iv_e) = \frac{\tau}{\rho H_e}, \tag{7}$$

where $u_e + iv_e$ is horizontal Ekman current in complex notation. Ignoring the contributions from the wind stress divergence (Geisler, 1970), the equation for the vertical velocity, w_e, at the base of Ekman layer is

$$\left(\frac{\partial^2}{\partial t^2} + f^2\right) w_e = \frac{f}{\rho} curl_z \tau. \tag{8}$$

Following the same approach in section 2.1, the steady Ekman pumping can be written for $t > t_0$ as

$$h_e = \frac{1}{\rho U f} \int_{-Ut_0}^{Ut_0} curl_z \tau dx, \tag{9}$$

where $h_e = \int_{-\infty}^{t} w_e dt$.

2.3. Wind Stress Profile and Analytical Solution

Because wind stress divergence of radial winds hardly has an effect on geostrophic response (Geisler, 1970; Price, 1983; Shay et al., 1989), in this study we only consider the oceanic response forced by an axisymmetric azimuthal wind field. A double-exponential parametric model proposed by Willoughby et al. (2006) is used for the TC wind field, which only needs the specification of the maximum wind speed (V_{max}) and the latitude (ϕ). In this model, the radius of maximum winds (R_m) is determined by V_{max} and ϕ. The wind stresses are then calculated by the bulk formula

$$\tau = \rho_a C_D V_\theta^2, \tag{10}$$

where $\rho_a = 1.26$ kg m^{-3} is the air density, V_θ is the azimuthal wind speed, and C_D is the drag coefficient. Since C_D levels off at high wind speeds (Donelan et al., 2004; Powell et al., 2003), we simply add a cap of 2.6×10^{-3} to the celebrated formula in Large and Pond (1981) to form C_D here, that is, $C_D = 10^{-3} \times \min[0.49 + 0.065V_\theta, 2.6]$. The typical parameters used here are $V_{max} = 35$ m s^{-1}, $\phi = 16.5°$ N, $R_m = 35.6$ km, $U = 13.2$ km hr^{-1}.

To examine the effect of the TC forcing, we define $F = \int_{-Ut_0}^{Ut_0} curl_z \tau dx$; where the contributions of the along-track and cross-track wind stresses are $F_x = \int_{-Ut_0}^{Ut_0} -\partial \tau_x / \partial y dx$ and $F_y = \int_{-Ut_0}^{Ut_0} \partial \tau_y / \partial x dx$, respectively. Both axisymmetric wind stresses and wind stress curl monotonically increase inside the TC eye wall and rapidly decrease outside it (Figure 2a). However, the integrated forcing F is approximately a constant for | $y| \leq R_m$ (Figure 2b), with F_y being infinitesimal and $F \approx F_x$ (Figure 2b); these corroborate the viewpoint of Ginis and Sutyrin (1995) that the geostrophic response is primarily generated by the steady Ekman upwelling associated with along-track wind stresses. To analytically solve Equation 5, we use a piecewise
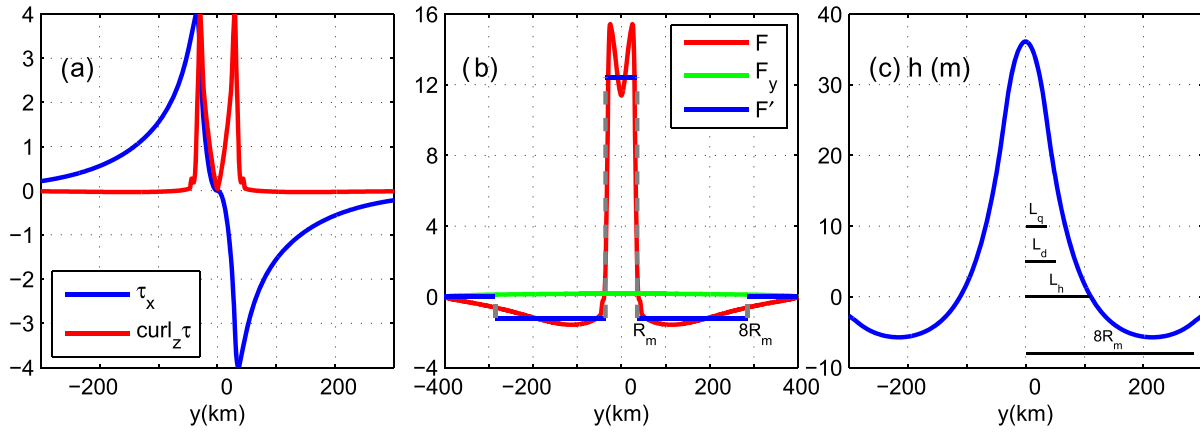
Figure 2. (a) Wind stress (N m^{-2}) and wind stress curl (10^{-4} N m^{-3}); (b) F (N m^{-2}), F_y (N m^{-2}), and the fitted forcing F' (N m^{-2}); (c) interface undulations by 13; serval length scales is plotted in (c) for clarity.

constant function F' to fit F that is numerically integrated from the wind stress curl in Figure 2a. The fitted function is given by

$$F' = \begin{cases} 3.1\tau_m, & |y| \le R_m \\ -0.3\tau_m, & R_m < |y| \le 8R_m \,, \\ 0, & |y| > 8R_m \end{cases} \tag{11}$$

where τ_m is the maximum wind stress. The coefficients in 11, 3.1 and -0.3, approximate the respective averages within the intervals $|y| \le R_m$ and $R_m < |y| \le 8R_m$.

For the piecewise forcing F', Equation 5 is a one-dimensional Helmholtz equation and can be solved by constructing Green's function (Duffy, 2015). The solution can be written as

$$h(y) = \frac{1}{2\rho UC}\int_{-\infty}^{\infty} F'(y')\exp\left(-\frac{|y - y'|}{L_d}\right)dy'. \tag{12}$$

Substituting 11 into 12, we obtain an analytic solution:

$$h = \begin{cases} \dfrac{\tau_m}{\rho Uf}\left[3.1 - 3.4\exp\left(-\dfrac{R_m}{L_d}\right)\cosh\left(\dfrac{|y|}{L_d}\right) + 0.3\exp\left(-\dfrac{8R_m}{L_d}\right)\cosh\left(\dfrac{|y|}{L_d}\right)\right], & |y| \le R_m \\[3mm] \dfrac{\tau_m}{\rho Uf}\left[3.4\sinh\left(\dfrac{R_m}{L_d}\right)\exp\left(-\dfrac{|y|}{L_d}\right) + 0.3\exp\left(-\dfrac{8R_m}{L_d}\right)\cosh\left(\dfrac{|y|}{L_d}\right) - 0.3\right], & R_m < |y| \le 8R_m \,, \\[3mm] \dfrac{\tau_m}{\rho Uf}\left[3.4\sinh\left(\dfrac{R_m}{L_d}\right)\exp\left(-\dfrac{|y|}{L_d}\right) - 0.3\sinh\left(\dfrac{8R_m}{L_d}\right)\exp\left(-\dfrac{|y|}{L_d}\right)\right], & |y| > 8R_m \end{cases} \tag{13}$$

the structure of which is shown in Figure 2c. Correspondingly, the steady Ekman pumping, h_e, under the forcing F' is

$$h_e = \begin{cases} 3.1\dfrac{\tau_m}{\rho Uf}, & |y| \le R_m \\[2mm] -0.3\dfrac{\tau_m}{\rho Uf}, & R_m < |y| \le 8R_m \cdot \\[2mm] 0, & |y| > 8R_m \end{cases} \tag{14}$$

2.4. Strength and Cross-Track Length Scale

Setting $y = 0$ in 13 gives the maximum upwelling,

$$h^{max} \approx \frac{\tau_m}{\rho U f} \left[3.1 - 3.4 \exp\left(-\frac{R_m}{L_d} \right) \right], \tag{15}$$

As seen from Figure 2c, the cross-track length scale of h, L_h, is estimated by the junction point of the upwelling and downwelling. Setting $h = 0$ in 13, we find

$$L_h \approx L_d \ln[11.3 \sinh(R_m/L_d)]. \tag{16}$$

To understand the parameter dependences in 15 and 16, we recall that the mass conservation in TC-induced upwelling is $\int_{-\infty}^{\infty} w_e dy = \int_{-\infty}^{\infty} w dy$ (i.e., $\int_{-\infty}^{\infty} h_e dy = \int_{-\infty}^{\infty} h dy$). This relation is easily verified by substitution from 13 and 14. From the term $\int_{-\infty}^{\infty} h_e dy$, we can see that the strength of the perturbation of the interface at the base of Ekman layer only depends upon parameters of the TC: $\tau_m R_m / U f$. Nevertheless, the thermocline response is also related to local stratification because the diffusion of h in the cross-track direction is dominated by L_d. For a fixed forcing, increasing L_d gives a larger L_h and smaller h^{max}.

For the parameters used here, $L_h \approx 110.0$ km, while the scale of h_e is $R_m = 35.6$ km. This implies that an expanded region of upwelling appears from the base of Ekman layer ($z = -H_e$) to the thermocline ($z = -H_1$). By contrast, the cross-track length scale of the PV injected into the thermocline, L_q, is also R_m. Later we will illustrate these two scales (L_h and L_q) are the most important scales of TC-induced perturbation to the underlying eddies.

3. Numerical Model and Methods

3.1. Model Configuration and Numerical Experiments

Configuration of numerical model is virtually the same as in LWS except that there are no preexisting COEs. The flat-bottomed, numerical, f plane, ocean model used here was configured based on the HYCOM model (Bleck, 2002). The KPP turbulence closure scheme of Large et al. (1994) was chosen to parameterize the vertical mixing. Because the geostrophic response is generated in the forced stage (section 2.1), the effect of interior vertical mixing associated with high mode internal wave shear (Meroni et al., 2017; Niwa & Hibiya, 1997) is in fact negligible. The model ocean basin was 4,000 m deep and uses 30 stretched vertical grids with the first grid interval being 10 m. The oceanic conditions in LWS were taken for the numerical experiments in this study. The initial quiescent ocean was driven by wind stresses only, and the oceanic stratification is set to the seasonal temperature/salinity field from the World Ocean Atlas 2009 (WOA09) near the location of the COE in LWS. The model's latitude was fixed at 16.5 ° N. In order to avoid reflected near-inertial wave energy from contaminating the simulated geostrophic response, we divide the computation domain into inner zone and an outer wave-damped zone. The inner zone covers the model domain of $(-1,000 \text{ km}, 2,000 \text{ km}) \times (-1,300 \text{ km}, 1,300 \text{ km})$ with a 10 km × 10 km uniform rectangle grid. The wave-damped zone extends 30 coarse grid points outside the inner zone in $-x$ and $\pm y$ directions to damp near-inertial waves. In addition to the above mesh technique, 10-grid point sponge layers were also introduced near the boundaries to suppress wave reflection.

The imposed forcing in the reference experiment was the same as that described in section 2.3. To examine the effect of the forcing strength, two groups of experiment trials were implemented. One group kept all other parameters unchanged and varied U from 5 to 35 km hr^{-1}. Similarly, the other group only varied V_{max} from 20 to 50 m s^{-1}. Because the effect of the oceanic stratification depends on the geographic location that a TC passes through, that effect was not considered here.

3.2. Methodology

The near-inertial response dominates the response in the two week period immediately after the passage of a TC (Shay & Elsberry, 1987). After the near-inertial waves disperse horizontally and vertically, only the geostrophic response remains. Because after it is generated, the geostrophic response does not change in the along-track direction (x), we applied a 42-hr (one inertial period) moving average as a low-pass filter to smooth the 3-hr simulated output over a cross-track section to obtain the geostrophic response variables. An extremely weak evolution still exists in the low-pass filtered geostrophic response probably due to

nonlinear processes. The section at $t = 15$ day was used to analyze vertical pattern of geostrophic response. The potential vorticity (PV) response was calculated in z coordinate grid by

$$q = -\frac{\zeta + f}{\rho}\frac{\partial \rho}{\partial z},\tag{17}$$

where ζ is relative vorticity. Then the grid calculated PV was interpolated onto the isopycnals at equal isopycnal intervals. Finally, the anomaly of PV (PVA) signal with respect to pre-TC PV field was computed.

Since the baroclinic response cannot perturb the local ocean over the entire water column, it is vital to determine how deep the geostrophic response can penetrate. The penetration depth of the response to mesoscale atmospheric forcing depends heavily on the local stratification and the forcing time (Orlanski & Polinsky, 1983). For simplicity, we defined the penetration depth in HYCOM output, D_{PV}, as the maximum depth given by

$$|PVA|_{y=0} \geq -\frac{\beta L_q}{\rho_0}\frac{\partial \rho_0}{\partial z},\tag{18}$$

where $|PVA|_{y=0}$ is PVA below the Ekman layer along the track, β is the gradient of planetary vorticity, ρ_0 is pre-TC density, and $L_q = 50$ km. The right-side of 18 denotes the PV contribution of the β effect; thus, 18 means the maximum depth where TC-induced PV contribution is larger than that of the β effect. Note that 18 is implemented on isopycnals and D_{PV} corresponds to the pre-TC maximum depth to which the TC response can penetrate.

3.3. Background Eddies

To examine the effects of a TC on the underlying eddies, we compared the TC-induced geostrophic perturbation with the eddy structure of a background COE or AOE derived from the $4^\circ \times 4^\circ$ Argo composite data set in Zhang et al. (2013). To do this, we picked a temperature/salinity profile, $T'(z)/S'(z)$, from the data set in the domain of (132°E, 136°E) × (18°N,22°N) that reflects the eddy-perturbed mean features in the oceanic region shown in Figure 1. After the eddy SSH extreme (η_{eddy}) of a COE or AOE is prescribed, the eddy-induced temperature/salinity perturbation of the background eddy is

$$T''(r, z) = \eta_{eddy}T'(z)\left[1 - 0.5(r/R)^2\right]exp\left[-0.5(r/R)^2\right],\tag{19a}$$

and

$$S''(r, z) = \eta_{eddy}S'(z)\left[1 - 0.5(r/R)^2\right]exp\left[-0.5(r/R)^2\right],\tag{19b}$$

where $R = 85$ km. Combining the eddy-induced perturbation (19) and the seasonal temperature/salinity field prescribed in HYCOM, we can obtain the temperature/salinity field of the background eddy. The geostrophic currents of the background eddy can then be calculated by use of the thermal-wind relation. Finally, to remain consistent with the simulated geostrophic response, the background eddy was implemented in HYCOM through a spin-up procedure without forcing. Note that this study considers the perturbed PV pattern of an eddy only by linear superposition. For simplicity, we did not use the TC forcing directly to simulate the response and evolution of the background eddy in HYCOM. The radius of positive (negative) PVA for a background COE (AOE) is about 100 km and extends down to a depth of over 1,000 m (Figure 3). The core with the largest positive (negative) PVA for a background COE (AOE) resides in a depth range of 100–180 m. For the background eddy-perturbed PVA, D_{PV} is in fact a representative scale of the eddy depth (Zhang et al., 2014) and is also calculated to compare with TC-induced perturbations.

4. The Simulated Geostrophic Response

4.1. Spatial Structure of the Geostrophic Response

Both the two-layer theory and numerical simulations show that the horizontal patterns of geostrophic response are a thermocline ridge with the maximum response centered on the TC track (Figure 4). In particular, if no low-pass filter is applied to the total theoretical response, the geostrophic component cannot be
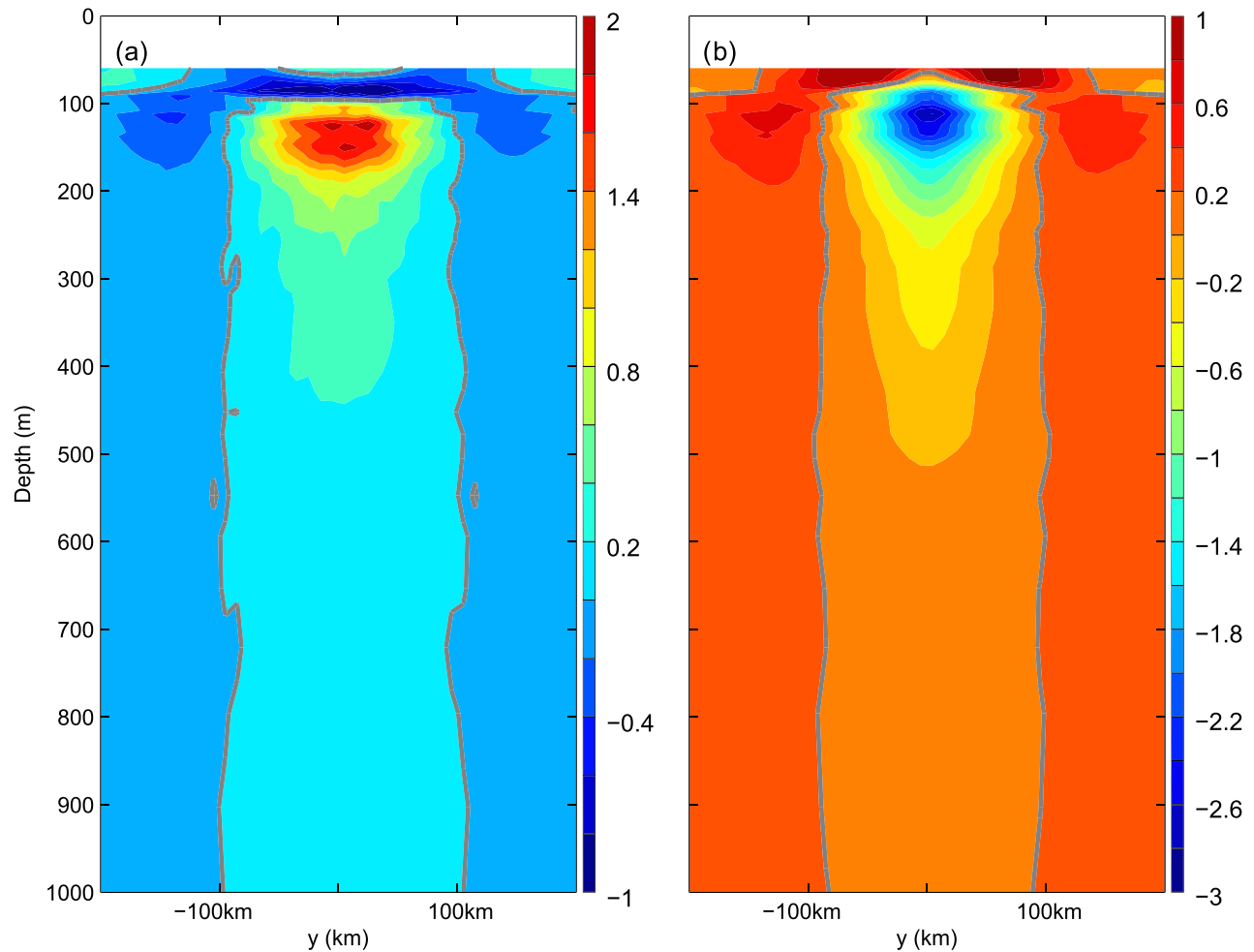
Figure 3. PVA (10^{-10} m^{-1}s^{-1}) of background COE (a) and AOE (b) with amplitudes of 15 cm. Note that the depth corresponds to the initial depth of unperturbed isopycnals and no data exist at depths shallower than 50 m.

discerned because it is entirely masked by the near-inertial response (Figure 4a). The temperature anomaly in Figure 4b is nearly identical to that obtained by a composite analysis of Argo data (Lin et al., 2017), which seems to capture the persistent features of the observed upwelling. The length scale of upwelling revealed in Figure 4b is about 75 km, which is smaller than that predicted by the formula 16. This is due to the fact that the scale of the upwelling expands from the base of Ekman layer to the thermocline with the width of upwelling varying significantly with depth.

As stated in section 1, in the deep ocean, altimetry-based observations of the SSH may serve as an ideal tool to identify the strength and length scale of baroclinic geostrophic response. Further, on an f plane, the barotropic and baroclinic SSH can be easily separated within the HYCOM output. The barotropic SSH is estimated by (Ginis & Sutyrin, 1995)

$$\overline{\eta}(y) = \int_{-\infty}^{y} -\frac{f\overline{u}(y')}{g} dy',$$ (20)

where $\overline{u}$ is the simulated along-track barotropic currents and g is the gravitational acceleration. The baroclinic component is then determined by subtracting this barotropic component from the total SSH response. An SSH trough is clearly visible in the total response with a length scale of approximately 130 km (Figure 5a). Obviously, both the barotropic and baroclinic SSH patterns manifest as along-track troughs, but with different magnitudes and length scales (Figures 5b and 5c). The maximum depression and length
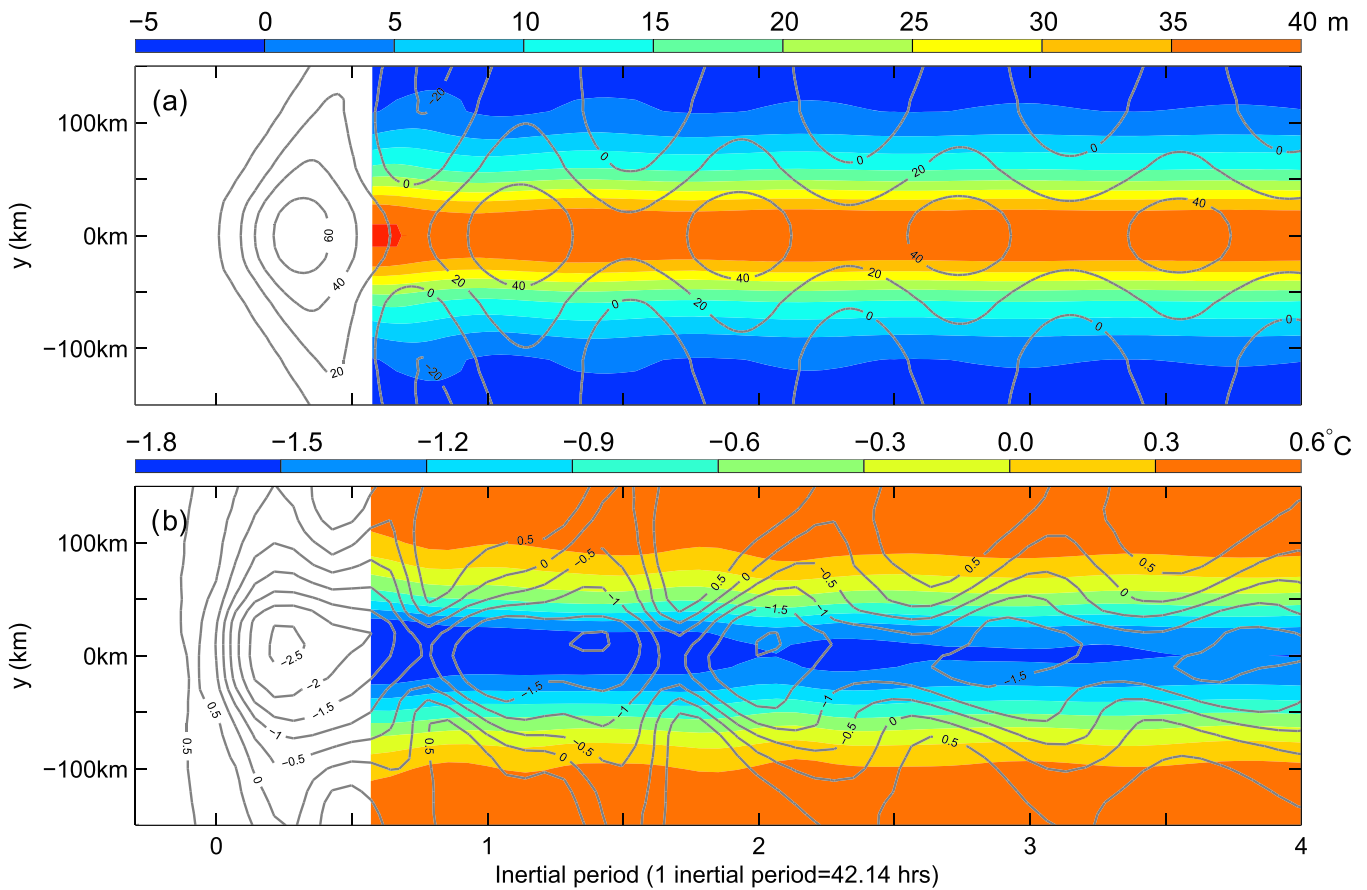
Figure 4. (a) Isopycnal undulations calculated by the two-layer theory. (b) the simulated temperature response by HYCOM at 150 m depth. Contour map denotes total response while color map denotes the geostrophic component of the response.

scale of baroclinic (barotropic) SSH are approximately -12.8 (-2.2) cm and 110 (600) km, respectively. The length scale of baroclinic component (~110 km) is slightly smaller than that (~130 km) of the total response since the weak barotropic component acts to widen the scale of total response. These simulated results show that the magnitude and length scale of geostrophic response in a deep ocean can be approximately estimated by altimetry-based measurements.

The cross-track temperature pattern shows upwelling under the TC and downwelling to its flanks (for | $y| > 100$ km; Figures 6a and 6b). The temperature response is symmetric about the storm track except for the rightward bias of sea surface cooling. The isopycnal undulations, represented by the isothermals in Figure 6a, are similar to the analytical solution in Figure 2c, whereas the width of upwelling varies with depth (Figure 6b). It is easily deduced that the along-track geostrophic currents and zero cross-track velocities should be accompanied with the along-track thermocline ridge (Figure 6c). The magnitudes of these geostrophic currents clearly decay with depth. If we judge the contributions of the geostrophic response by these currents, the effect of the TC is roughly confined within $|y| < 150$ km and $z > -200$ m. As predicted in section 2.1, positive PVA is injected into the thermocline (Figure 6d). Below the base of Ekman layer, the width of this positive PVA injection is initially narrow, and it expands slightly as depth increases. The length scale of the positive PVA injection zone is about 50 km, close to the value of R_m indicated in (6) and (11). The maximum TC-injected PVA appears at 160 m depth on the track. Here, $D_{PV} \approx 250$ m, suggesting that the effect of TC-induced PVA is confined in a thin layer between $-D_{PV} < z < -H_e$. Compared to the background PVA in Figure 3, for -200 m $< z < -H_e$, the magnitude of TC-induced PVA exceeds that of the background eddies. By contrast, the TC-induced PVA for $z < -200$ m is smaller than that of the background eddies and becomes negligible for $z < -D_{PV}$.
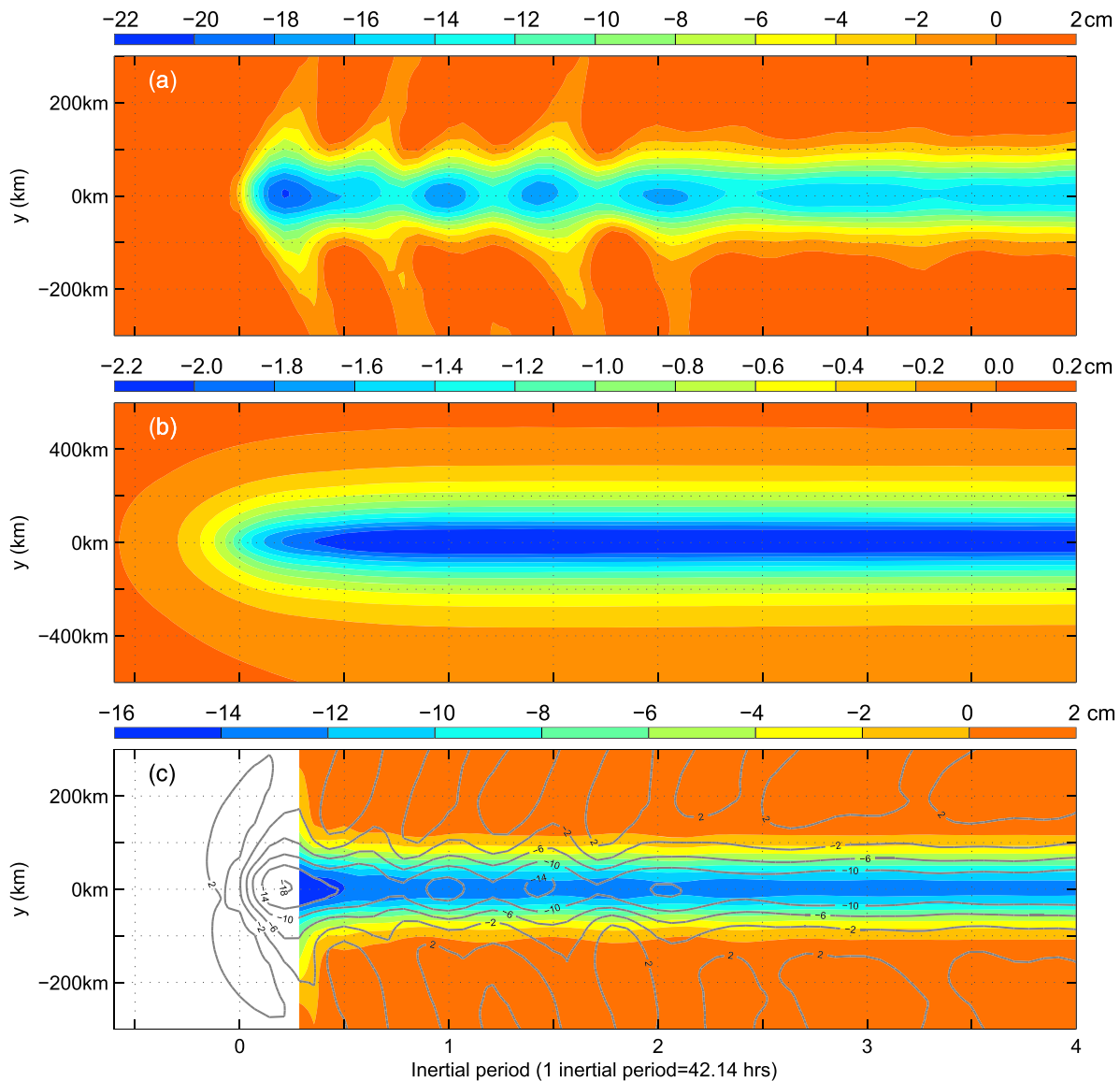
Figure 5. Simulated SSH (cm). (a) Total response; (b) barotropic component; (c) baroclinic geostrophic response (color) and baroclinic total response (contour).

Due to the similarity of the geostrophic response along the TC track, the structure of the geostrophic response is essentially a vertical pattern, which is schematically described in Figure 7 based on upwelling. This pattern can be roughly separated into three layers: the Ekman layer, an expansionary layer, and a contractive layer. In the expansionary layer, both the PVA and upwelling are significant while in contractive layer upwelling is still perceptible but the PVA signal is negligible. Below the contractive layer (or roughly $z < -500$ m in Figure 6b where the maximum cooling is less than 0.1 °C), both the upwelling and PVA signals are negligible. A TC first generates steady upwelling in the Ekman layer. Subsequently, an expansionary upwelling zone forms below the Ekman layer because surrounding seawater compensates for the Ekman pumping not only from the zone under the Ekman suction but also from the water on both sides of the storm track. As depth increases, the Ekman pumping decays and only the upwelling near the track is maintained with the off-track upwelling gradually disappearing. Clearly, the length scale revealed in baroclinic SSH (Figure 5c) is the mean width of upwelling in the expansionary layer. The TC-induced positive PV injection occurs in the expansionary layer and the SSH response detected from altimetry-based measurement mainly reflects the upwelling in the expansionary layer. The upwelling in the Ekman and expansionary layer can be
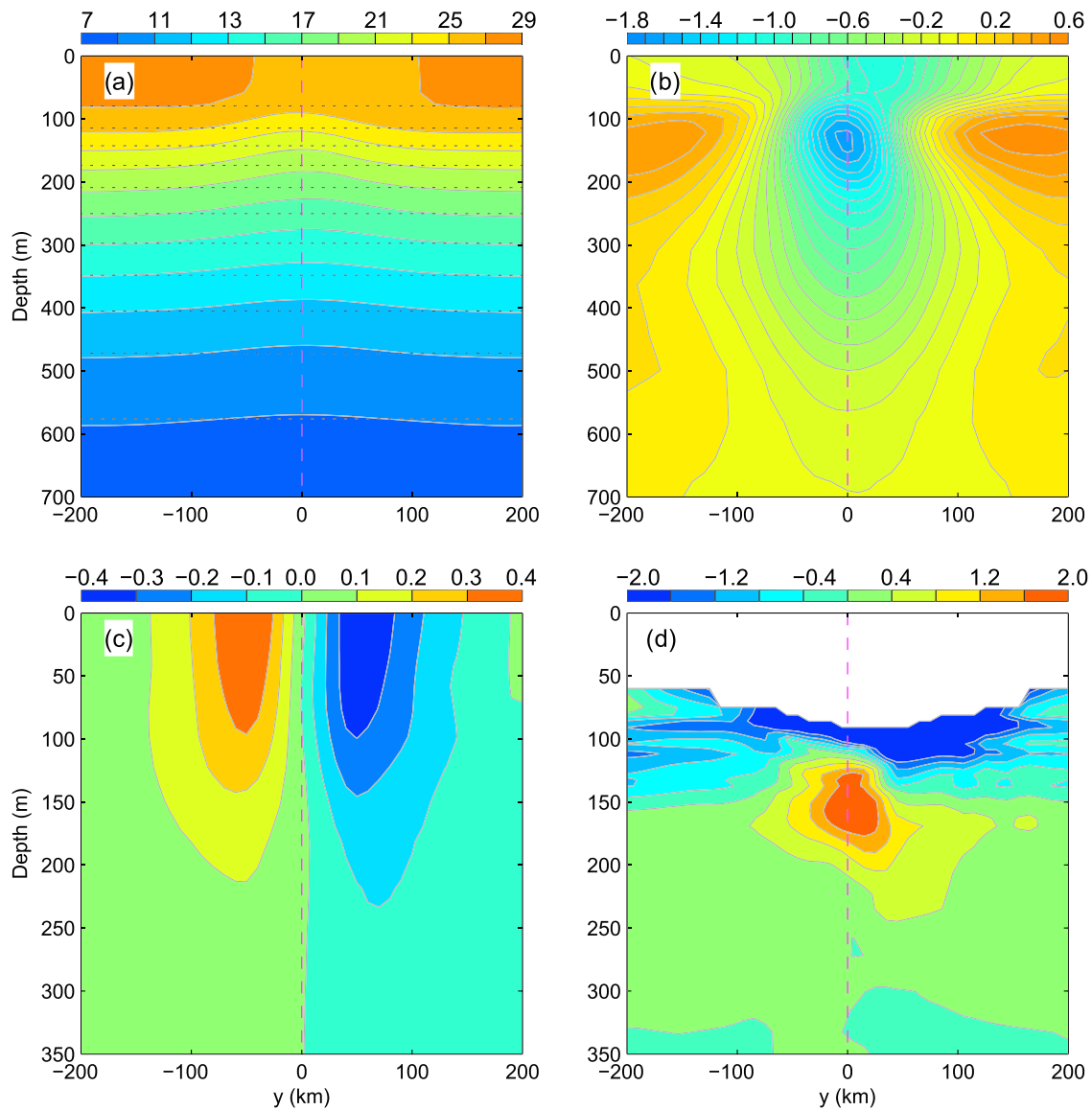
Figure 6. Vertical pattern of the simulated geostrophic response. (a) Temperature response (°C), here horizontal dashed lines denote initial temperature; (b) temperature anomaly (°C); (c) along-track geostrophic currents (m s^{-1}); (d) PVA (10^{-10} m^{-1}s^{-1}). The pink dashed line for $y = 0$ is plotted to illustrate the symmetry of the response about the track of the TC. The depth in (d) corresponds to the initial depth of unperturbed isopycnals and TC-induced surface mixing enables no PVA data in well-mixed layer.

characterized by equations 14 and 13, respectively. Theoretically, the length scale at the base of Ekman layer should be R_m; however, it is perceivably larger than R_m because of the presence of weak stratification at the base of Ekman layer. Similar to the process in a two-layer model, this weak stratification causes upwelling at the base of Ekman layer to slightly diffuse laterally, increasing the width above R_m.

4.2. Comparisons Between Geostrophic Response and Eddies

The TC forcing in the reference experiment is relatively stronger in realistic TCs due to higher V_{max} and slower U, so it is not surprising that the response in section 4.1 is well comparable to the underlying eddies. It is very important to see whether a general TC can significantly perturb an existing general eddy. According to 16, the length scale of geostrophic response, roughly 100 km, is insensitive to the strength of a TC and is of same order as eddy radius. However, as shown in section 2.4, the strength of geostrophic response is dominated by the TC parameter $\tau_m R_m / Uf$. Since the effect of geographic location including the changes of latitude
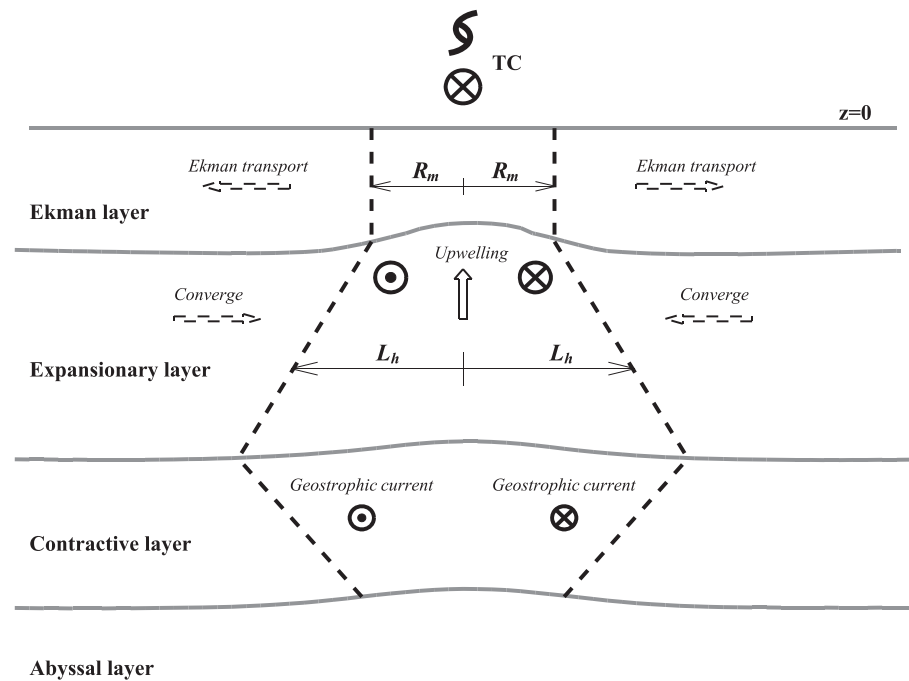
Figure 7. Schematic description of geostrophic upwelling.

and local stratification is too complicated and the variations of R_m is relatively small, here we have only investigated the effect of V_{max} and U on the strength of the geostrophic response (Figure 8).

The simulated maximum SSH depression confirms that the strength of the SSH response changes with V_{max}^2/U (Figures 8a and 8b). Further, all length scales identified from the simulated SSH response are approximately 130–150 km (figures not shown) and insensitive to the forcing strength. Analysis of altimetry-based SSH fields show that the global mean amplitude and radius of ocean eddies are roughly 8 cm and 90 km, respectively (Chelton et al., 2011). Even for a low intensity TC with a relatively high moving speed, the maximum SSHA depression of about 5 cm is also comparable with that of the amplitude of the weakest eddies (Chelton et al., 2011; Xu et al., 2016). Thus, in comparison with the amplitude and radius of the underlying eddies, the strength and length scale of the geostrophic response permits a TC to inject a remarkable perturbation to the underlying ocean eddy field.

To illustrate the vertical discrepancy between the geostrophic response and background eddies, maximum undulations ($|h|^{max}$) on the $\sigma = 24$ isopycnal surface and D_{PV} are compared with those of background eddies possessing the same maximum SSH depressions and shown in Figures 8c–8f. It is unsurprising that maximum undulations reflect the same strength change as maximum SSH depressions (Figures 8c and 8d). As the forcing weakens, the positive PV injection, which can only penetrate to at most 300 m, shows an obvious decrease in the penetration depth (Figures 8e and 8f). Since PV is injected into a thinner layer between $-D_{PV} < z < -H_e$, the thickness narrows as the forcing weakens. When compared to the depth scale of the background eddies (approximately 1,000 m) revealed by D_{PV} (Figures 8e and 8f), the thin layer of PV injection is always far smaller than the vertical range of the background eddies. Interestingly, Figures 8c and 8d show that the TC-induced isopycnal undulations are always 1.5–1.8 times those of background eddies possessing the same maximum SSH depression. This suggests that significant TC-induced upwelling mainly appears in the thin thermocline.

The simulated evolution of the COE in LWS confirms that the initial perturbation to the COE by Typhoon Lupit occurs in a thin layer around the thermocline and the COE below the thermocline is not initially affected. However, after the passage of the TC, the 3D structure of the eddy adjusts following the perturbed thermocline. Another potential effect of the vertical structure of the TC-induced perturbations is that
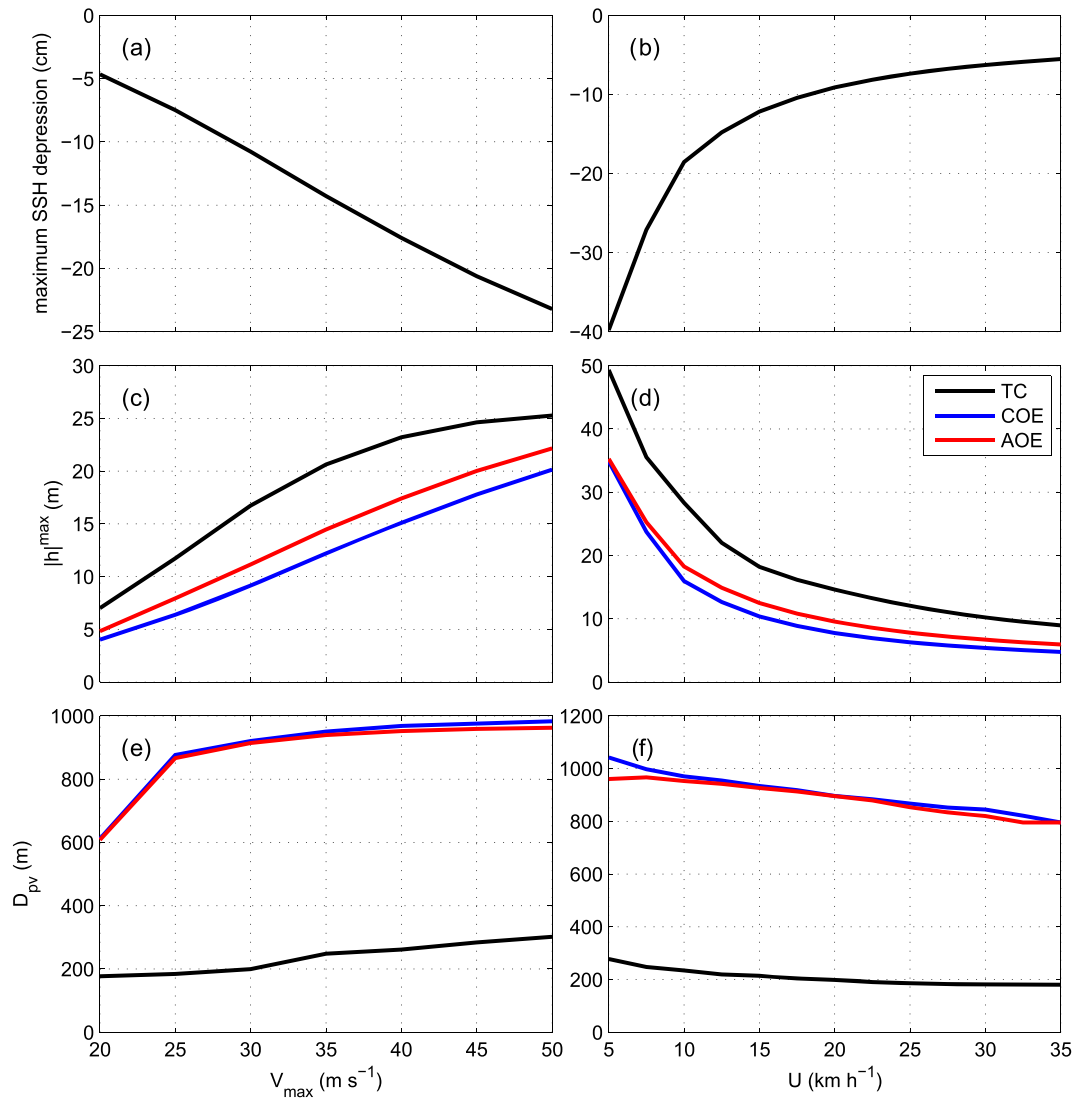
Figure 8. Change in the geostrophic response as a function of maximum wind speed (the left column) and TC moving speed (the right column). (a,b) The maximum SSH (cm) depression; (c,d) $|h|^{max}$ (m) ; (e,f) D_{PV} (m). $|h|^{max}$ and D_{PV} of background COE and AOE is estimated in eddy model 20 by prescribing the corresponding maximum SSH depression in (a) and (b).

TC-generated COEs, for example, C3 and C4 in Figure 1, may only have a maximum eddy depth of 300 m, inferred from D_{PV} in Figures 8e and 8f.

5. The Perturbed Eddies

5.1. Conceptual Model for the Perturbed Eddies

The PV and upwelling changes associated with the geostrophic response are essentially linear and injected into the thermocline, while the underlying eddies are also linear and satisfy geostrophic balance. Therefore, the TC-induced perturbations can be conceptually described by a linear combination of PV and geostrophic streamfunction (upwelling) in the thermocline, that is,

$$q = q_{TC} + q_{eddy} \text{ and } \psi = \psi_{TC} + \psi_{eddy}, \tag{21}$$

where ψ is geostrophic streamfunction and the subscript "TC" and "eddy" denote the TC-induced and the
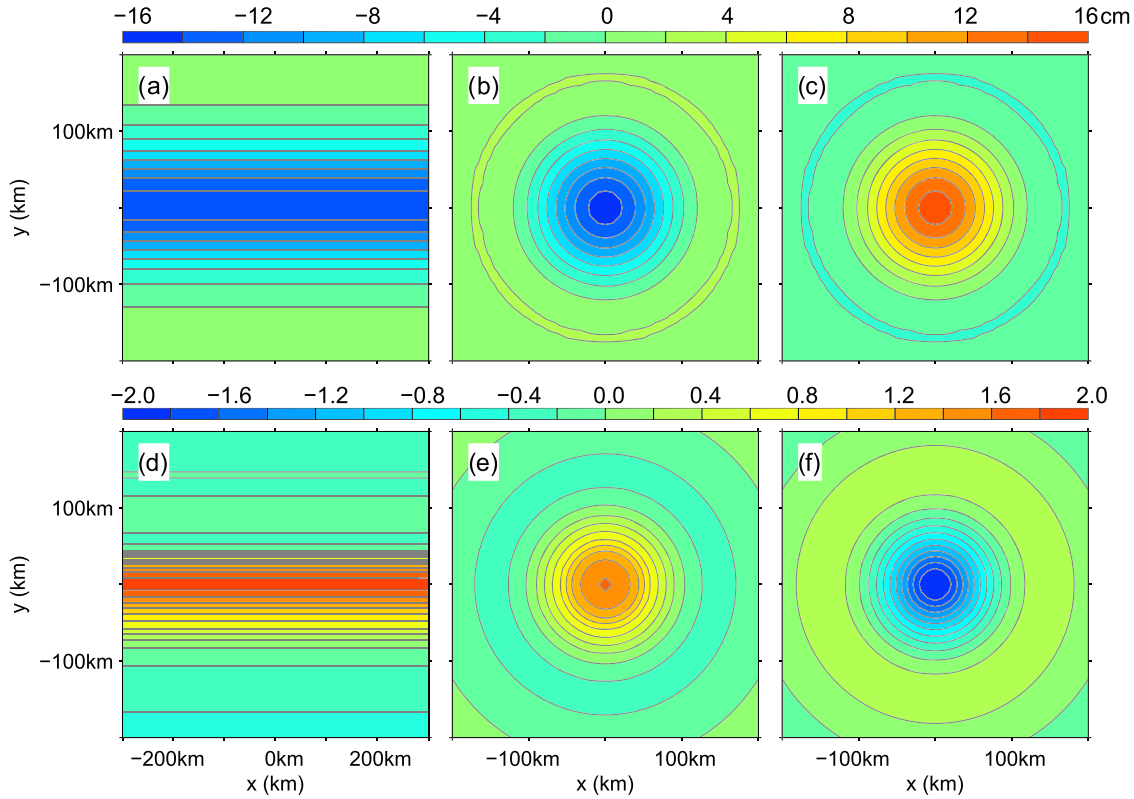
Figure 9. Perturbed ψ (a) and initial ψ of background COE (b) and AOE (c), all of which are conceptually represented by SSH (cm). The perturbed q (d) and initial q (10^{-10} m^{-1}s^{-1}) on the $\sigma = 24$ isopycnal surface for COE (d) and AOE (f).

preexisting eddy components, respectively. After the underlying eddies have been perturbed by a TC, their 3D evolution must maintain PV conservation:

$$\frac{\partial q}{\partial t} + J(\psi, q) = 0, \tag{22}$$

where J is the Jacobian determinant. On an f plane, if there are no TC-induced perturbations, this evolution does not occur. However, TC-induced PV provides extra dynamical sources to perturb the thermocline, and as a consequence of 22, the unperturbed eddy part must adjust to the TC-induced changes of the thermocline. The following discussion only considers the adjustment in the thermocline. Since $J(\psi_{TC}, q_{TC}) \approx 0$ and $J(\psi_{eddy}, q_{eddy}) \approx 0$, 22 is rewritten to

$$\frac{\partial q}{\partial t} + J\left(\psi_{TC}, q_{eddy}\right) + J\left(\psi_{eddy}, q_{TC}\right) = 0. \tag{23}$$

In the context of two-layer model, $\psi = -g'h/f = g\eta/f$, so that the distribution of ψ is equivalent to that of SSH. The horizontal pattern of ψ_{TC} and q_{TC} in the thermocline is conceptually illustrated in Figure 9. Clearly, the contours of TC-induced perturbations are parallel with the track, while those of background eddies are concentric circles. If background eddies are not far away from the TC track, $J(\psi_{TC}, q_{eddy}) \neq 0$ and $J(\psi_{eddy}, q_{TC}) \neq 0$ always influence the perturbed eddies driving them to evolve and adjust. Note that the length scale of ψ_{TC} is not equal to that of q_{TC} (i.e., $L_h \neq L_q$), which means that the eddy-TC separation distance, s, will be a crucial factor that regulates the evolution of the perturbed eddies as described by 21.

5.2. The Perturbed Patterns for Different s

The perturbation patterns for different s inferred from the conceptual model (Figure 10) can be divided into three regions: $|s| \leq S_1$, $S_1 < |s| \leq S_2$, and $|s| > S_2$, where $S_1 \approx 80$ km and $S_2 \approx 150$ km. This rough division is
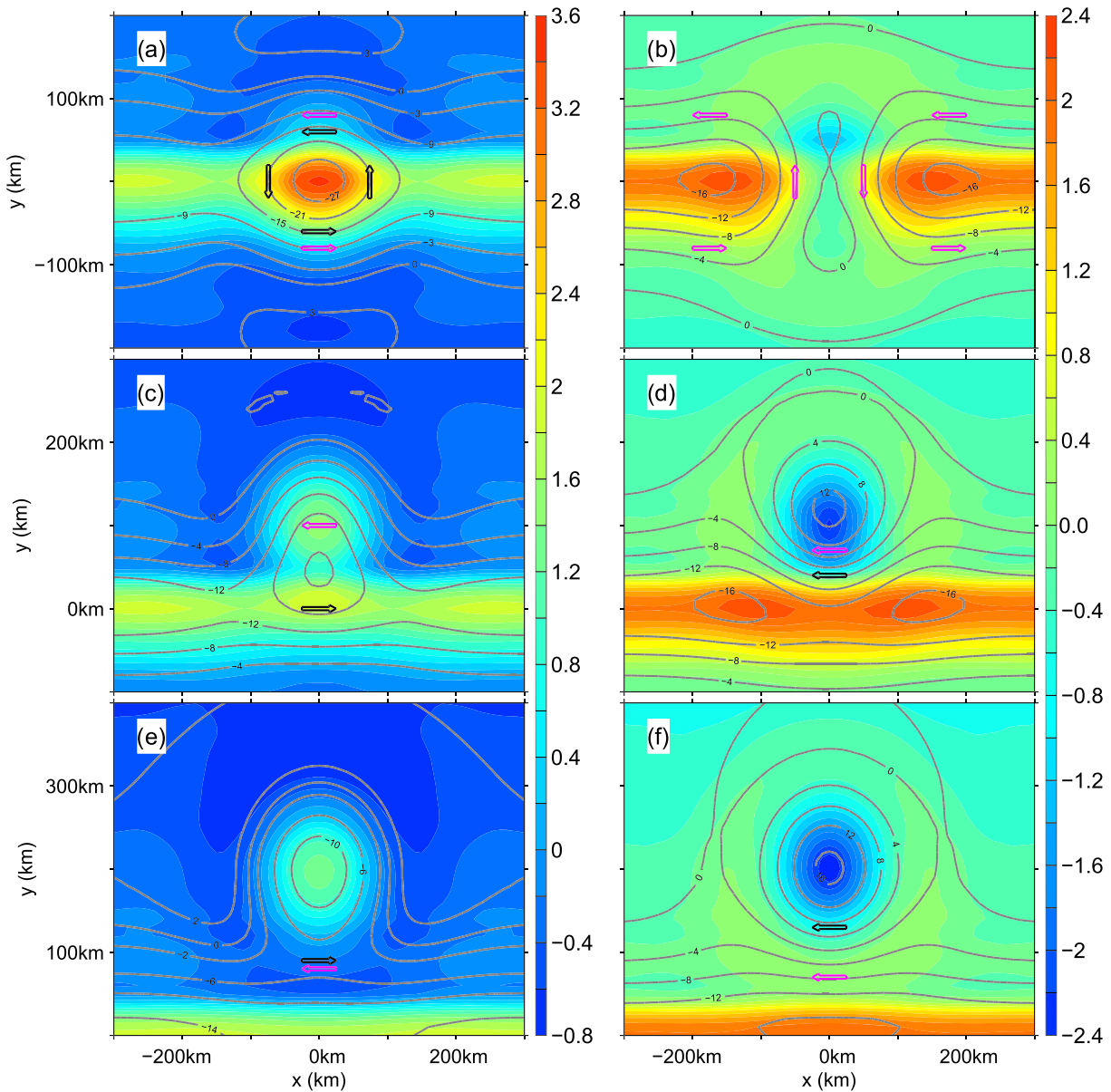
Figure 10. Perturbed patterns described by conceptual model. The color map denotes q (10^{-10} m^{-1}s^{-1}) on the $\sigma = 24$ isopycnal surface while the contour of SSH (cm) denotes the patterns of ψ. The left column is for COE and the right for AOE. Three planes are for $s = 0,100,200$ km. The black and pink arrows denote $J(\psi_{eddy}, q_{TC})$ and $J(\psi_{TC}, q_{eddy})$, respectively.

based upon the different combinations of physical processes acting in these regions. Note that the magnitudes of S_1 and S_2 are closely linked to the scales of the geostrophic response and the underlying eddies. In Figure 10, we ignore the slight right-left asymmetry due to nonlinear advection and only consider eddies that lie on the right side of a TC track. The features of the three regions are discussed as follows:

$$|s| \leq S_1.$$

Both the PV and isopycnal uplift of the background COE are enhanced in this case (Figure 10a). A typical example was the COE perturbed by Typhoon Lupit discussed in LWS. The elliptical deformation of the COE with an along-track long axis can be ascribed to the along-track TC-induced upwelling. The cyclonic

rotation of the perturbed COE in LWS can be very easily interpreted by $J(\psi_{eddy}, q_{TC})$. However, contrary to Typhoon Lupit's effect on the COE, the perturbed AOE is weakened from both the PV and isopycnal undulations (Figure 10b). Interestingly, the geostrophic wakes are pinched off by the preexisting AOE and form two COEs in front of and to the rear of the AOE. The circular preexisting AOE also incurs elliptical deformation and its long axis is perpendicular to the track of the typhoon. Meanwhile, the AOE is weakened or destroyed, depending on the strength of the TC forcing. This can be seen from perturbed SSH patterns of A1 and A2 in Figure 1c.

$$S_1 < |s| \leq S_2.$$

In this case, even though isopycnal undulations are still perturbed, the initial PV fields of the background eddies are not remarkably affected by TC-induced PV. In Figure 10c, both $J(\psi_{TC}, q_{eddy})$ and $J(\psi_{eddy}, q_{TC})$ drive the positive PV of the preexisting COE to absorb the TC-induced positive PV injection. By contrast, the negative PV of the preexisting AOE does not interact with TC-induced positive PV injection and the eddy is merely advected by the geostrophic wakes (Figure 10d).

$$|s| > S_2.$$

With the increase of $|s|$, the perturbations including PV and uplift tend to vanish (Figures 10e and 10f), which cannot be discerned from altimetry-based SSH observations. However, the geostrophic currents in the thermocline shown in Figure 6c decrease from about 7 cm s^{-1} at $|y| = 150$ km to 3 cm s^{-1} at $|y| = 200$ km. In this range of geostrophic currents, the advection of $J(\psi_{TC}, q_{eddy})$ seems to be still comparable with the β-induced westward eddy movement (Chelton & Schlax, 1996). However, this process remains uncertain because the distribution of geostrophic currents depends heavily on the radial profile of the TC wind field and the forcing strength.

6. Conclusions

A TC perturbs the underlying eddy field through the geostrophic response. Consequently, the features of the geostrophic response play a key role in the long-term effects of TC-induced changes on the mesoscale and large-scale ocean circulation. Improving our understanding of the dynamics of these processes will provide a clearer picture of the role that TCs play in ocean circulation. This study has examined the strength, horizontal scales, and vertical range of upwelling and PV injection linked to the geostrophic response to a TC based on a two-layer theoretical model and an OGCM. Furthermore, these features were compared to those of background eddies to highlight the significant contribution of the TC-induced geostrophic response.

Compared to the altimetry-based observations of amplitude and radius of oceanic eddies, the strength (5- to 40-cm maximum SSH depression) and cross-track length scale (approximately 130 km) of TC-induced geostrophic response can have long-term effects on the underlying eddy field. It is found that the geostrophic response is primarily confined to the thin thermocline between 100 and 300 m depth, and this vertical feature dominates the 3D evolution of the perturbed eddies.

Based on the horizontal scales of upwelling and injected PV, a conceptual model was presented to interpret the perturbation to an eddy by a TC as a function of the eddy-TC separation distance. Overall, when an eddy is located within ± 80 km of the TC track, the perturbation is more significant, while an eddy outside of ± 200 km of the TC track will be essentially unaffected.

To our knowledge, this study is the first endeavor to address the spatial features of the geostrophic response induced by a TC. Our results give a comprehensive physical picture of the TC-induced perturbation to both COEs and AOEs as a function of cross-track location. However, this study is only the first step in understanding the long-term effects of TCs on the mesoscale eddy field and the general circulation. More work should be done to investigate the evolution of the perturbed eddy field and the attendant biophysical processes.

References

Benilov, E. S. (2005). On the stability of oceanic vortices: A solution to the problem? *Dynamics of Atmospheres and Oceans*, *40*(3), 133–149. http://www.sciencedirect.com/science/article/pii/S0377026505000059

Bleck, R. (2002). An oceanic general circulation model framed in hybrid isopycnic-Cartesian coordinates. *Ocean Modelling*, *4*(1), 55–88. http://www.sciencedirect.com/science/article/pii/S1463500301000129

Carton, X. (2001). Hydrodynamical modeling of oceanic vortices. *Surveys in Geophysics*, *22*(3), 179–263. https://doi.org/10.1023/A%3A1013779219578

Chelton, D. B., & Schlax, M. G. (1996). Global observations of oceanic Rossby waves. *Science*, *272*(5259), 234. https://doi.org/10.1126/science.272.5259.234, http://science.sciencemag.org/content/272/5259/234.abstract

Chelton, D. B., Schlax, M. G., & Samelson, R. M. (2011). Global observations of nonlinear mesoscale eddies. *Progress in Oceanography*, *91*(2), 167–216.

Cohen, Y., Dvorkin, Y., & Paldor, N. (2015). Linear instability of constant PV cold-core eddies in a two-layer ocean. *Quarterly Journal of the Royal Meteorological Society*, *141*(692), 2886–2897. https://doi.org/10.1002/qj.2575

Cohen, Y., Dvorkin, Y., & Paldor, N. (2016). On the stability of outcropping eddies in a constant-PV ocean. *Quarterly Journal of the Royal Meteorological Society*, *142*(698), 1920–1928. https://doi.org/10.1002/qj.2785

Dibarboure, G., Lauret, O., Mertz, F., Rosmorduc, V., & Maheu, C. (2010). SSALTO/DUACS user handbook:(M) SLA and (M) ADT near-real time and delayed time products CLS-DOS-NT-06.034 Iss 2.1.

Donelan, M. A., Haus, B. K., Reul, N., Plant, W. J., Stiassnie, M., Graber, H. C., et al. (2004). On the limiting aerodynamic roughness of the ocean in very strong winds. *Geophysical Research Letters*, *31*, L18306. https://doi.org/10.1029/2004GL019460

Duffy, D. (2015). *Green's functions with applications* (Second ed.). Boca Raton, FL: CRC Press.

Emanuel, K. A. (1991). The theory of hurricanes. *Annual Review of Fluid Mechanics*, *23*(1), 179–196.

Geisler, J. E. (1970). Linear theory of the response of a two layer ocean to a moving hurricane‡. *Geophysical and Astrophysical Fluid Dynamics*, *1*(1–2), 249–272.

Gill, A. (1982). *Atmosphere-ocean dynamics*. San Diego, CA: Academic Press.

Gill, A. (1984). On the behavior of internal waves in the wakes of storms. *Journal of Physical Oceanography*, *14*(7), 1129–1151.

Ginis, I. (2002). Tropical cyclone-ocean interactions. Atmosphere-Ocean Interactions, Advances in Fluid Mechanics Series, No. 33, WIT Press, 83-114.

Ginis, I., & Sutyrin, G. (1995). Hurricane-generated depth-averaged currents and sea surface elevation. *Journal of Physical Oceanography*, *25*(6), 1218–1242. https://doi.org/10.1175/1520-0485(1995)025<1218:HGDACA>2.0.CO;2

Gordon, A. L., Shroyer, E., & Murty, V. S. N. (2017). An intrathermocline eddy and a tropical cyclone in the Bay of Bengal. *Scientific reports*, *7*. https://doi.org/10.1038/srep46218

Greatbatch, R. J. (1984). On the response of the ocean to a moving storm: Parameters and scales. *Journal of Physical Oceanography*, *14*(1), 59–78. https://doi.org/10.1175/1520-0485(1984)014<0059:OTROTO>2.0.CO;2

Jaimes, B., & Shay, L. K. (2009). Mixed layer cooling in mesoscale oceanic eddies during Hurricanes Katrina and Rita. *Monthly Weather Review*, *137*(12), 4188–4207. https://doi.org/10.1175/2009MWR2849.1

Jaimes, B., & Shay, L. K. (2010). Near-inertial wave wake of Hurricanes Katrina and Rita over mesoscale oceanic eddies. *Journal of Physical Oceanography*, *40*(6), 1320–1337. https://doi.org/10.1175/2010JPO4309.1

Jaimes, B., & Shay, L. K. (2015). Enhanced wind-driven downwelling flow in warm oceanic eddy features during the intensification of tropical cyclone Isaac (2012): Observations and theory. *Journal of Physical Oceanography*, *45*(6), 1667–1689.

Kudryavtsev, V., Monzikova, A., Combot, C., Chapron, B., Reul, N., & Quilfen, Y. (2019). A simplified model for the baroclinic and barotropic ocean response to moving tropical cyclones: 1. Satellite observations. *Journal of Geophysical Research: Oceans*, *124*, 3446–3461. https://doi.org/10.1029/2018JC014746

Large, W. G., McWilliams, J. C., & Doney, S. C. (1994). Oceanic vertical mixing: A review and a model with a nonlocal boundary layer parameterization. *Reviews of Geophysics*, *32*(4), 363–403. https://doi.org/10.1029/94RG01872

Large, W. G., & Pond, S. (1981). Open ocean momentum flux measurements in moderate to strong winds. *Journal of Physical Oceanography*, *11*(3), 324–336. https://doi.org/10.1175/1520-0485(1981)011<0324:OOMFMI>2.0.CO;2

Lin, I., Wu, C.-C., Emanuel, K. A., Lee, I.-H., Wu, C.-R., & Pun, I.-F. (2005). The interaction of Supertyphoon Maemi (2003) with a warm ocean eddy. *Monthly Weather Review*, *133*(9), 2635–2649.

Lin, S., Zhang, W.-Z., Shang, S.-P., & Hong, H.-S. (2017). Ocean response to typhoons in the western North Pacific: Composite results from Argo data. *Deep Sea Research Part I: Oceanographic Research Papers*, *123*, 62–74. http://www.sciencedirect.com/science/article/pii/S0967063716302874

Lu, Z., Wang, G., & Shang, X. (2016). Response of a preexisting cyclonic ocean eddy to a typhoon. *Journal of Physical Oceanography*, *46*(8), 2403–2410. https://doi.org/10.1175/JPO-D-16-0040.1

Meroni, A. N., Miller, M. D., Tziperman, E., & Pasquero, C. (2017). Nonlinear energy transfer among ocean internal waves in the wake of a moving cyclone. *Journal of Physical Oceanography*, *47*(8), 1961–1980. https://doi.org/10.1175/JPO-D-16-0232.1

Nilsson, J. (1995). Energy flux from traveling hurricanes to the oceanic internal wave field. *Journal of Physical Oceanography*, *25*(4), 558–573.

Niwa, Y., & Hibiya, T. (1997). Nonlinear processes of energy transfer from traveling hurricanes to the deep ocean internal wave field. *Journal of Geophysical Research*, *102*(C6), 12,469–12,477. https://doi.org/10.1029/97JC00588

Orlanski, I., & Polinsky, L. J. (1983). Ocean response to mesoscale atmospheric forcing. *Tellus A: Dynamic Meteorology and Oceanography*, *35*(4), 296–323. https://doi.org/10.3402/tellusa.v35i4.11441

Pedlosky, J. (2003). *Waves in the ocean and atmosphere: Introduction to wave dynamics*. New York: Springer-Verlag Berlin Heidelberg.

Powell, M. D., Vickery, P. J., & Reinhold, T. A. (2003). Reduced drag coefficient for high wind speeds in tropical cyclones. *Nature*, *422*(6929), 279–283. https://doi.org/10.1038/nature01481

Price, J. F. (1983). Internal wave wake of a moving storm. Part I. Scales, energy budget and observations. *Journal of Physical Oceanography*, *13*(6), 949–965. https://doi.org/10.1175/1520-0485(1983)013<0949:IWWOAM>2.0.CO;2

Price, J. F., Sanford, T. B., & Forristall, G. Z. (1994). Forced stage response to a moving hurricane. *Journal of Physical Oceanography*, *24*(2), 233–260. https://doi.org/10.1175/1520-0485(1994)024<0233:FSRTAM>2.0.CO;2

Shang, X.-D., Zhu, H.-B., Chen, G.-Y., Xu, C., & Yang, Q. (2015). Research on cold core eddy change and phytoplankton bloom induced by typhoons: Case studies in the South China Sea. *Advances in Meteorology*, *2015*, 1–19. https://doi.org/10.1155/2015/340432

Shay, L. K., Chang, S. W., & Elsberry, R. L. (1990). Free surface effects on the near-inertial ocean current response to a hurricane. *Journal of Physical Oceanography*, *20*(9), 1405–1424. https://doi.org/10.1175/1520-0485(1990)020<1405:FSEOTN>2.0.CO;2

Shay, L. K., & Elsberry, R. L. (1987). Near-inertial ocean current response to Hurricane Frederic. *Journal of Physical Oceanography*, *17*(8), 1249–1269.

Shay, L. K., Elsberry, R. L., & Black, P. G. (1989). Vertical structure of the ocean current response to a hurricane. *Journal of Physical Oceanography*, *19*(5), 649–669.

Shay, L. K., Goni, G. J., & Black, P. G. (2000). Effects of a warm oceanic feature on Hurricane Opal. *Monthly Weather Review*, *128*(5), 1366–1383. https://doi.org/10.1175/1520-0493(2000)128<1366:EOAWOF>2.0.CO;2

Sun, L., Li, Y.-X., Yang, Y.-J., Wu, Q., Chen, X.-T., Li, Q.-Y., et al. (2014). Effects of super typhoons on cyclonic ocean eddies in the western North Pacific: A satellite data-based evaluation between 2000 and 2008. *Journal of Geophysical Research: Oceans*, *119*, 5585–5598. https://doi.org/10.1002/2013JC009575

Sun, L., Yang, Y.-J., Xian, T., Wang, Y., & Fu, Y.-F. (2012). Ocean responses to Typhoon Namtheun explored with Argo floats and multi-platform satellites. *Atmosphere-Ocean*, *50*, 15–26.

Walker, N. D., Leben, R. R., Pilley, C. T., Shannon, M., Herndon, D. C., Pun, I. F., et al. (2014). Slow translation speed causes rapid collapse of Northeast Pacific Hurricane Kenneth over cold core eddy. *Geophysical Research Letters*, *41*, 7595–7601. https://doi.org/10.1002/2014GL061584

Willoughby, H. E., Darling, R. W. R., & Rahn, M. E. (2006). Parametric representation of the primary hurricane vortex. Part II: A new family of sectionally continuous profiles. *Monthly Weather Review*, *134*(4), 1102–1120. https://doi.org/10.1175/MWR3106.1

Xu, C., Zhai, X., & Shang, X.-D. (2016). Work done by atmospheric winds on mesoscale ocean eddies. *Geophysical Research Letters*, *43*, 12,174–112,180. https://doi.org/10.1002/2016GL071275

Zhang, Z., Wang, W., & Qiu, B. (2014). Oceanic mass transport by mesoscale eddies. *Science*, *345*(6194), 322–324. http://www.ncbi.nlm.nih.gov/pubmed/25035491, https://doi.org/10.1126/science.1252418

Zhang, Z., Zhang, Y., Wang, W., & Huang, R. X. (2013). Universal structure of mesoscale eddies in the ocean. *Geophysical Research Letters*, *40*, 3677–3681. https://doi.org/10.1002/grl.50736

Zheng, Z.-W., Ho, C.-R., Zheng, Q., Lo, Y.-T., Kuo, N.-J., & Gopalakrishnan, G. (2010). Effects of preexisting cyclonic eddies on upper ocean responses to Category 5 typhoons in the western North Pacific. *Journal of Geophysical Research*, *115*, C09013. https://doi.org/10.1029/2009JC005562